

Decoupling polarization and coercive field in AlScN/AlN/AlScN stack for enhanced performance in ferroelectric thin-film transistors

Received: 20 May 2025

Accepted: 4 August 2025

Published online: 11 August 2025



Kyung Do Kim¹, Seung Kyu Ryoo¹, Min Kyu Yeom¹, Suk Hyun Lee¹, Wonho Choi¹, Yunjae Kim^{1,2}, Jung-Hae Choi², Tianjiao Xin³, Yan Cheng³ & Cheol Seong Hwang¹✉

AlScN emerges as a promising material for ferroelectric field-effect transistors due to its high coercive field (>6 MV/cm). However, its high remanent polarization (>100 $\mu\text{C}/\text{cm}^2$) can degrade memory window and retention, limiting its use in memory applications. This study introduces an AlScN/AlN/AlScN multi-layer designed to decouple the polarization and coercive field, thereby increasing the coercive field while maintaining polarization value. The AlN layer switches ferroelectrically in response to the AlScN layer's switching, even though a single AlN layer is piezoelectric. The lower dielectric constant of AlN compared to AlScN increases the coercive field of the stack, while the AlScN layer primarily determines the polarization. This study shows that increasing the AlN ratio in the multi-layer significantly enhances the memory window and retention performance of ferroelectric thin-film transistors with amorphous indium-gallium-zinc-oxide channels. A maximum memory window of 15 V is achieved, enabling the development of a penta-level cell for next-generation storage.

NAND flash memory, the dominant current storage solution, stores data through charge trapping in silicon nitride, known as charge trap nitride (CTN)^{1–3}. CTN-based NAND has increased storage capacity through multiple-bit operation and vertically stacking memory cells. However, these approaches are reaching physical and architectural limits, such as cell-to-cell interference and vertical pitch scaling challenges, necessitating the development of alternative memory technologies^{4,5}.

Ferroelectric field-effect transistors (FeFETs) have emerged as promising candidates for next-generation non-volatile memory^{6,7}. However, FeFETs face challenges due to a limited memory window (MW) that is constrained to twice the coercive voltage ($2V_C$) of the

ferroelectric layer. This limitation is especially pronounced in fluorite-structured ferroelectrics due to their low coercive field (E_C , ~ 1 MV/cm)^{8–10}. Moreover, their multiphase nature and randomly oriented grains lead to a broad distribution of E_C across domains. Consequently, FeFETs using fluorite ferroelectrics experience interference between adjacent cells during program (PGM) and erase (ERS) operations⁶.

To overcome these challenges, aluminum scandium nitride (AlScN) has emerged as a promising ferroelectric for FeFETs due to its high E_C (>6 MV/cm), superior thermal stability, and improved switching uniformity compared to fluorite ferroelectrics^{11–14}. However, AlScN-based FeFETs still suffer from a limited MW that progressively degrades over time, particularly when the AlScN film thickness is

¹Department of Materials Science and Engineering and Inter-University Semiconductor Research Center, Seoul National University, Seoul, South Korea.

²Electronic Materials Research Center, Korea Institute of Science and Technology, Seoul, South Korea. ³Key Laboratory of Polar Materials and Devices (MOE), Department of Electronics, East China Normal University, Shanghai, China. ✉e-mail: cheolsh@snu.ac.kr

scaled down^{15,16}. These issues are primarily attributed to strong depolarization fields induced by AlScN's high remanent polarization ($P_r > 100 \mu\text{C}/\text{cm}^2$)¹⁷.

To mitigate depolarization-related degradation, the E_C of ferroelectric material should be increased without increasing P_r ^{6,17,18}. However, E_C and P_r are intrinsically coupled in AlScN films. For example, reducing the Sc concentration increases E_C but also increases P_r ^{11,19,20}. This trade-off highlights the need for innovative strategies to decouple E_C and P_r , enabling their independent optimization.

This study proposes an AlScN/AlN/AlScN multi-layer structure to address these issues. Notably, the AlN film exhibits proximity-induced ferroelectric switching when incorporated between AlScN layers. By increasing the AlN ratio, E_C increased without altering P_r , enabling independent optimization of these parameters and leading to improved device performance.

Leveraging this approach, ferroelectric thin-film transistors (FeTFTs) are fabricated with an amorphous indium-gallium-zinc-oxide (a-IGZO) channel and an AlScN/AlN/AlScN multi-layer gate stack. Increasing the AlN ratio in the 40 nm-thick multi-layer improves the MW to -15 V with no degradation in retention. This improvement enables demonstration of penta-level-cell (PLC) operation using the incremental-step-pulse-programming (ISPP) method. These results establish the AlScN/AlN/AlScN multi-layer as a promising structure for high-density, reliable FeTFTs.

Results

Decoupling P_r and E_C in AlScN/AlN/AlScN multi-layer structure

Figure 1a shows the schematic diagram of sputter-grown $\text{HfN}_{0.4}$ /AlScN/AlN/AlScN/TiN capacitor structure, where $\text{HfN}_{0.4}$ serves as the bottom electrode (BE) due to its minimal lattice mismatch with AlScN²¹. The Sc concentration (x) in $\text{Al}_{1-x}\text{Sc}_x\text{N}$ film was fixed

at 0.2, otherwise indicated. All films were deposited without breaking vacuum, ensuring a well-crystallized structure. The total multi-layer thickness was fixed at 40 nm, with the AlN thickness (t_{AlN}) varying between 0 (single-layer AlScN) and 40 nm (single-layer AlN). “Single-layer” refers to a film that exists as an individual layer, not a multi-layer.

Figure 1b shows θ - 2θ X-ray diffraction (XRD) patterns, confirming that AlN and AlScN films exhibit $\langle 0002 \rangle$ orientations aligned in the out-of-plane direction. The (0002) XRD peak of the AlN single-layer is located at a higher 2θ angle than the AlScN single-layer, which can be attributed to the higher compressive residual stress in AlScN compared to AlN. For a 40 nm thickness, AlScN and AlN films exhibited residual stresses of -1.9 and -1.3 GPa, respectively. However, the overlap of the (0002) peaks of AlScN and AlN with the (10-11) peak of $\text{HfN}_{0.4}$ near 35.5° makes it challenging to resolve each peak position accurately. Therefore, high-resolution transmission electron microscopy (HRTEM) analysis was performed to investigate the AlScN film strain within the multi-layer structure.

Supplementary Fig. 1a shows an HRTEM image of the $\text{HfN}_{0.4}$ /AlScN/AlN/AlScN/TiN sample ($t_{\text{AlN}} = 18 \text{ nm}$), along with fast Fourier transform (FFT) patterns. FFT analysis confirms a well-aligned $\langle 0002 \rangle$ texture in AlScN and AlN films. Additionally, all films exhibited clear separation without interdiffusion and low oxygen concentrations (Supplementary Fig. 1b). Supplementary Fig. 1c, d shows the HRTEM image of the AlScN single-layer and AlScN/AlN/AlScN multi-layer, respectively. FFT patterns were obtained from the marked regions, and the (0002) lattice planes were reconstructed using inverse FFT. The d-spacing value of (0002) AlScN is identical between the single-layer and multi-layer configurations. These findings confirm that the strain state of the AlScN film is not significantly affected by the multi-layer structure.

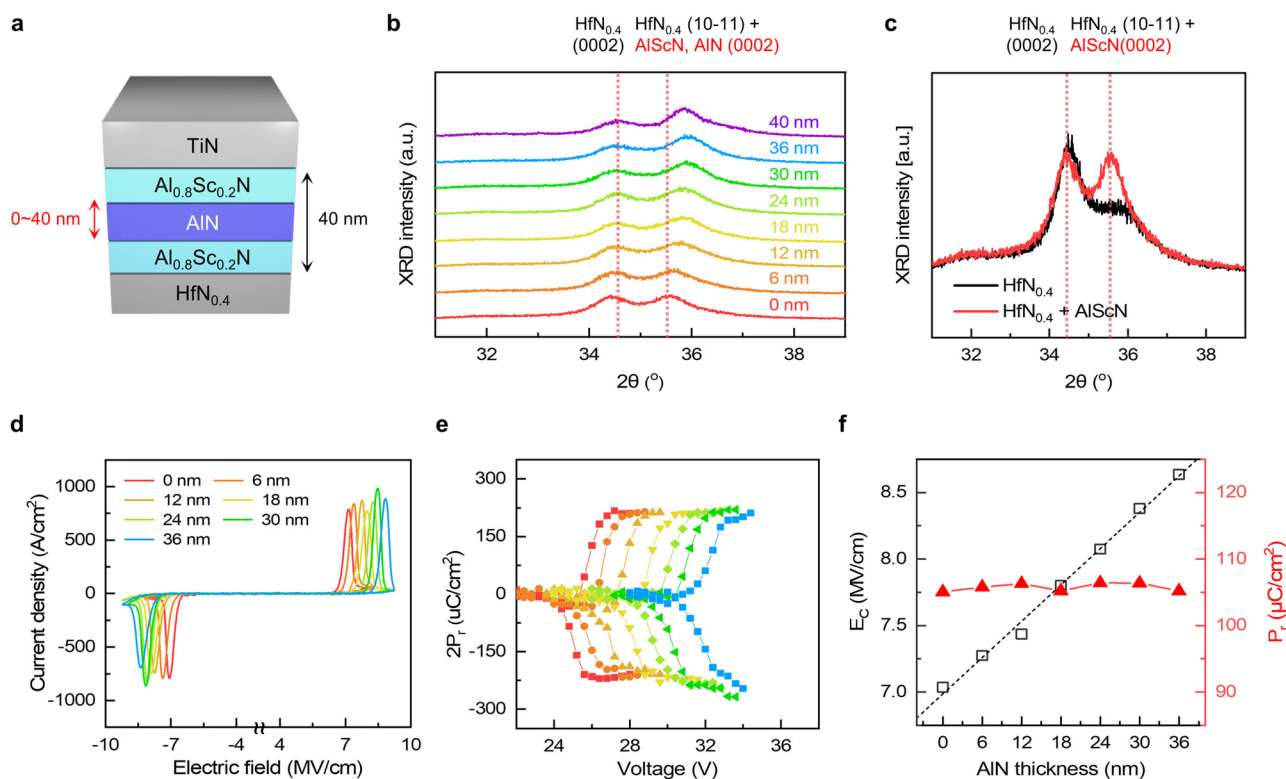


Fig. 1 | Characterizations of the $\text{HfN}_{0.4}$ /AlScN/AlN/AlScN/TiN structure.

a Schematic illustration of $\text{HfN}_{0.4}$ /AlScN/AlN/AlScN/TiN capacitors. **b** θ - 2θ X-ray diffraction (XRD) patterns of samples with varying t_{AlN} from 0 to 40 nm. t_{AlN} represents the AlN film thickness in the multi-layer. **c** θ - 2θ XRD patterns of $\text{HfN}_{0.4}$ bottom electrode (black line) and 40 nm-thick AlScN film/ $\text{HfN}_{0.4}$ bottom electrode

(red line). **d** Current density–electric field curves obtained using 50 kHz triangular PUND measurements. **e** $2P_r$ –voltage curves measured through 1- μs -width square pulse PUND measurements. **f** Variations in E_C and P_r of the multi-layer as a function of t_{AlN} .

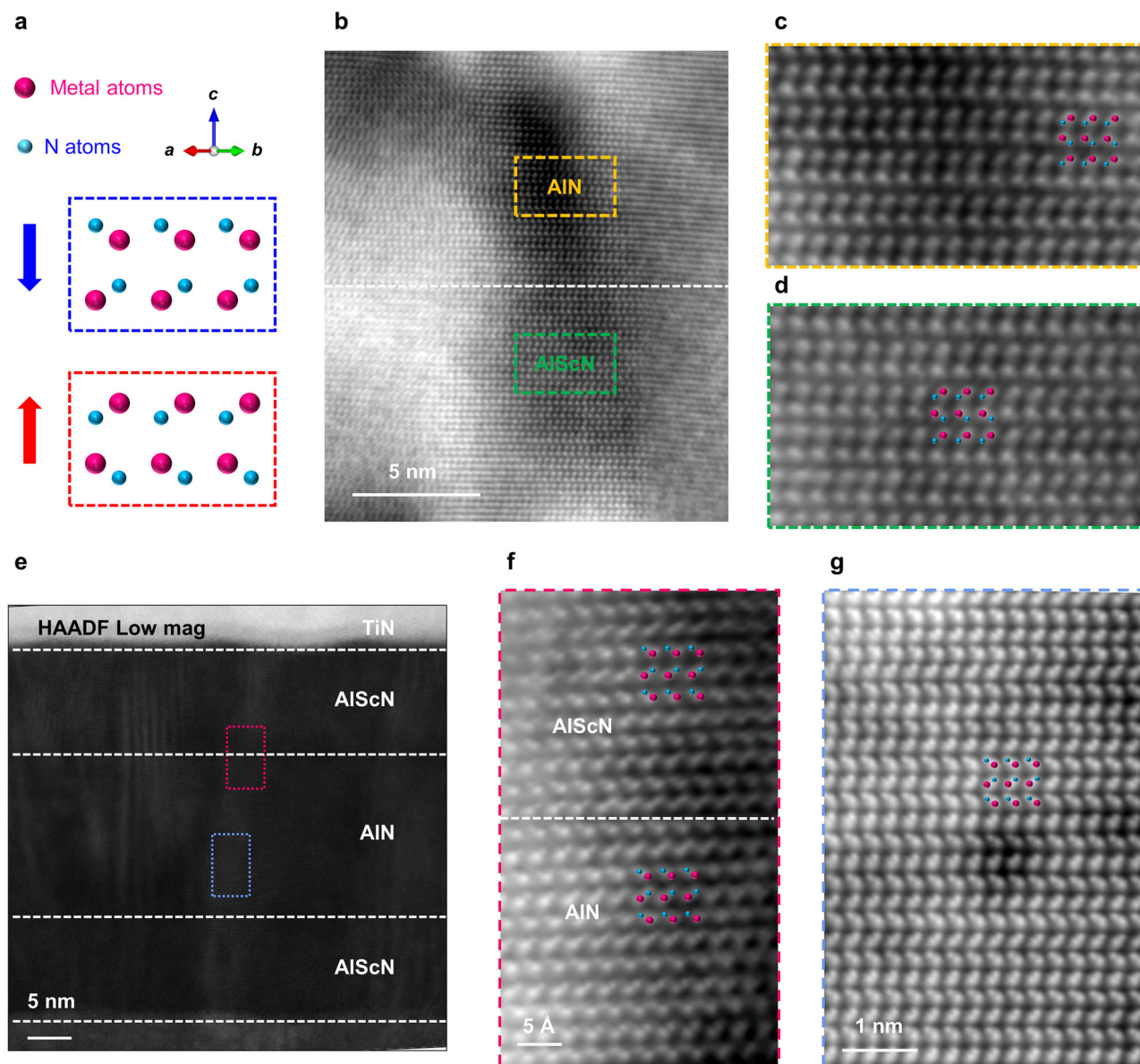


Fig. 2 | Polarity determination of AlScN and AlN films via STEM analysis.

a Variations in the atomic structure of AlScN based on polarization direction, captured along the $\langle 11\bar{2}0 \rangle$ crystallographic direction. **b** Cross-sectional integrated differential phase contrast (iDPC)-scanning transmission electron microscopy (STEM) image of the AlN/bottom-AlScN interface. Magnified iDPC-STEM images of

the **c** AlN and **d** AlScN films, with atomic structures represented by spheres (red for metal, blue for nitrogen). **e** Cross-sectional high-angle annular dark field (HAADF)-STEM overview of the specimen poled in the downward direction. Magnified iDPC-STEM images of the **f** AlN/top-AlScN interface and **g** AlN film. The polarization directions of the AlN and AlScN films align with the poling direction.

Supplementary Fig. 2 shows the variation in surface roughness of AlScN/AlN/AlScN multi-layers with different t_{AlN} . Due to the continuous growth of both AlScN and AlN layers in the wurtzite structure, multi-layers exhibited low surface roughness below 0.5 nm, regardless of the t_{AlN} .

Figure 1d shows the current density–electric field (J – E) curves of the multi-layer, measured using the positive-up-negative-down (PUND) method with 50 kHz triangular pulses. Ferroelectric switching occurred across all samples regardless of t_{AlN} . However, the 40 nm-thick AlN film broke down before ferroelectric switching due to an extremely high switching barrier¹⁹. AlScN/AlN bilayer stacks also showed ferroelectric switching, but exhibited excessive leakage currents at specific biases due to asymmetric interfaces (Supplementary Fig. 3)²². Therefore, this study adopted the symmetric AlScN/AlN/AlScN multi-layer structure.

Figure 1e shows the $2P_r$ –voltage ($2P_r$ – V) curves, measured using 1- μs -width square pulses, revealing P_r remained constant at $\sim 105 \mu\text{C}/\text{cm}^2$

regardless of t_{AlN} . In contrast, E_C increased linearly with t_{AlN} , from $\sim 7.0 \text{ MV}/\text{cm}$ ($t_{\text{AlN}} = 0 \text{ nm}$) to $\sim 8.6 \text{ MV}/\text{cm}$ ($t_{\text{AlN}} = 36 \text{ nm}$). Changes in ferroelectric properties with t_{AlN} are discussed in detail below.

Next, scanning transmission electron microscopy (STEM) in integrated differential phase contrast (iDPC) mode was employed to investigate whether the polarization of the AlN layer in a multi-layer could be reversed. Figure 2a illustrates atomic models of down- and up-poled wurtzite structures along the $\langle 11\bar{2}0 \rangle$ crystallographic direction.

First, the polarization state of the pristine film was analyzed. The polarization direction of AlScN and AlN in the pristine state could vary depending on deposition conditions, such as the concentration of oxygen impurity and substrate material^{23,24}. J – E curves were analyzed by applying two consecutive PUND pulses to the $\text{Hf}_{0.4}\text{N}/\text{AlScN}/\text{TiN}$ capacitor in the pristine state to determine the initial polarization direction (Supplementary Fig. 4a). During the first PUND pulse (black

curve), no ferroelectric switching was observed even under sufficiently high positive bias. However, switching occurred under a negative bias, indicating downward polarization in the pristine state. In the second PUND pulse (red curve), switching was observed under both bias polarities, confirming that the first pulse had switched the initial downward polarization. In addition, Supplementary Fig. 4b shows the high-angle annular dark field (HAADF) STEM image of the multi-layer ($t_{\text{AlN}} = 18$ nm) sample and iDPC-STEM image of the AlN layer, confirming that the AlN domains are also polarized downward.

The multi-layer capacitor was polarized upward by applying -36 V to the top electrode (TE) while grounding the BE. Figure 2b shows the iDPC-STEM image at the AlN/bottom-AlScN interface, and Fig. 2c, d provides magnified views of the AlN and AlScN regions, respectively. STEM analysis confirms that both AlN and AlScN films exhibit an upward polarization.

The multi-layer was subsequently polarized downward by applying $+36$ V to the TE, followed by STEM analysis. Figure 2e shows the HAADF STEM image of the sample. Figure 2f, g shows iDPC-STEM images of the top-AlScN/AlN interface and the AlN film, respectively, confirming the downward polarization in both AlScN and AlN films.

The alignment of the AlN's polarization with the poling direction demonstrates ferroelectric switching in the AlN film within the multi-layer, contrary to its non-ferroelectric behavior in single-layer configurations.

The STEM analysis of the AlScN/AlN/AlScN structure provided direct evidence that ferroelectric switching occurred in both AlScN and AlN layers. These findings align with the recently reported proximity-induced ferroelectricity phenomenon described by Skidmore et al.²⁵. Their study demonstrated that domain walls nucleated in a ferroelectric layer generated elastic and electric fields at a non-ferroelectric interface, effectively lowering the switching barrier of the non-ferroelectric layer and enabling its switching. Similarly, the switching in the AlScN layer in this work lowered the switching barrier of the adjacent AlN layer, allowing it to switch without breakdown.

Next, the switching performance of the multi-layer was compared with that of the single-layer AlScN film. In the multi-layer structure, although varying the t_{AlN} effectively alters the overall Sc content, the P_r remained nearly constant. This behavior contrasts with the single-layer AlScN, where the Sc concentration has a significant influence on ferroelectric properties^{11,19,20}. Supplementary Fig. 5a, b shows $J-E$ and $2P_r-V$ curves of AlScN films with different Sc concentrations. Increasing the Sc concentration led to a decrease in both E_C and P_r , along with a broader E_C distribution.

In polycrystalline AlScN, the ferroelectric switching dynamics could be explained using the inhomogeneous field mechanism (IFM) model detailed in Supplementary Note 1^{26–28}. Figure 3a shows the E_{loc} distribution extracted from the IFM model, fitted to a Gaussian distribution. E_{app} , E_{loc} , and $f(E_{\text{loc}}/E_{\text{app}})$ represent the applied electric field, the local electric field at each domain, and the E_{loc} distribution function, respectively. The standard deviation of the E_{loc} distribution increased from 0.04 to 0.09 as the Sc concentration increased from 0.2 to 0.3 (see Supplementary Figs. 6 and 7 and Supplementary Table 1).

In contrast, such changes were not observed in the multi-layer when varying the t_{AlN} for a given Sc concentration in the AlScN films. For example, E_{loc} distribution remained unchanged, showing the intrinsic properties of the AlScN film regardless of t_{AlN} (Fig. 3b). Similarly, P_r showed no dependence on t_{AlN} (Fig. 3c, Supplementary Fig. 5). These results indicate that in the multi-layer structure, P_r and E_{loc} distribution are determined by the AlScN film's characteristics.

Conversely, E_C increased linearly with t_{AlN} , with a steeper slope observed as Sc concentration in the AlScN film increased (Fig. 3c, Supplementary Fig. 5). This linear increase in E_C could be attributed to the lower dielectric constant of AlN (ϵ_{AlN}) compared to AlScN (ϵ_{AlScN})²⁹. Figure 3d shows the polarization–voltage ($P-V$) curves of the AlScN

and AlN films measured with low voltage to avoid ferroelectric switching. The slope corresponds to the dielectric constant of each layer ($\epsilon_{\text{AlN}} = 10.1$, $\epsilon_{\text{AlScN}} = -12.8$ – 17.0), and the $\epsilon_{\text{AlN}}/\epsilon_{\text{AlScN}}$ decreased with increasing Sc concentration.

If ferroelectric switching occurs when the electric field applied to the AlScN film within the multi-layer reaches its coercive field ($E_{C,\text{AlScN}}$), the E_C of the multi-layer could be expressed by Eq. 1³⁰.

$$E_C = E_{C,\text{AlScN}} \left(\frac{40 - t_{\text{AlN}}}{40} \right) + \frac{\epsilon_{\text{AlScN}}}{\epsilon_{\text{AlN}}} E_{C,\text{AlScN}} \left(\frac{t_{\text{AlN}}}{40} \right) \quad (1)$$

$$= \frac{E_{C,\text{AlScN}}}{40} \left(\frac{\epsilon_{\text{AlScN}}}{\epsilon_{\text{AlN}}} - 1 \right) t_{\text{AlN}} + E_{C,\text{AlScN}}$$

This equation confirms that the E_C of the multi-layer increases linearly with t_{AlN} , and the slope derived from Eq. 1 matched the slope observed in the E_C – t_{AlN} graph in Fig. 3c. These findings indicate ferroelectric switching in the multi-layer is initiated when the electric field applied to the AlScN film reaches $E_{C,\text{AlScN}}$. Consequently, while the E_C is linearly proportional to t_{AlN} , the ferroelectric properties, such as P_r and the E_{loc} distribution, remain consistent with those of the AlScN film. Therefore, the multi-layer structure enables the selective modulation of E_C by varying the AlN ratio, while maintaining a constant P_r . This behavior is summarized in Fig. 3e, where the multi-layer samples deviate from the typical linear P_r – E_C trend observed in single-layer AlScN^{11,19,31,32}.

However, it must be noted that Eq. 1 is valid only when the total multi-layer thickness is fixed (in this case, 40 nm). The E_C of the single-layer AlScN film increases with decreasing thickness²¹. However, the continuous growth of the AlScN and AlN films compensates for the $E_{C,\text{AlScN}}$ variation in the multi-layer, thereby making the $E_{C,\text{AlScN}}$ in the multi-layer constant in Eq. 1. When the total multi-layer thickness varies, the $E_{C,\text{AlScN}}$ will vary, resulting in different E_C values of the multi-layer stack. Details of this aspect will be reported elsewhere.

A similar decoupling effect might also be achieved in other multi-layer structures by interposing a switchable layer with a lower dielectric constant between the ferroelectric layers. A feasible candidate is $(\text{Hf}_{0.5}\text{Zr}_{0.5})\text{O}_2/\text{HfO}_2/(\text{Hf}_{0.5}\text{Zr}_{0.5})\text{O}_2$ multi-layer because the polar orthorhombic phase (o-phase) HfO_2 exhibits a higher switching barrier and lower dielectric constant than the o-phase $(\text{Hf}_{0.5}\text{Zr}_{0.5})\text{O}_2$ ^{33,34}. However, the metastable nature of the o-phase makes it challenging to observe this effect in the multi-layer structure, as detailed in the Supplementary Note 2 and Supplementary Fig. 8. The interposed HfO_2 film in the middle changed the entire structure to the nonpolar monoclinic phase. This finding indicates the unique property of the AlScN/AlN/AlScN multi-layer structure for achieving the goal of this work.

Enhancing the performance of a-IGZO FeTFT using AlScN/AlN/AlScN multi-layer gate stack

Next, a-IGZO ($\text{In:Ga:Zn} = 1:1:1$) FeTFTs were fabricated to evaluate the feasibility of the multi-layer structure for data storage applications. Figure 4a illustrates the schematic diagram of the a-IGZO/AlScN FeTFT. The total thickness of the multi-layer was fixed at 40 nm, with the t_{AlN} varying between 0 and 30 nm (see “Methods” for details on device fabrication). When the t_{AlN} value increased up to 36 nm, an excessive thickness, significant degradation in both P_r and endurance of the multi-layer capacitor was observed, as shown in Supplementary Fig. 9. It was reported that the interface of the AlScN film could be damaged during field cycling, resulting in the formation of a non-switchable layer²⁷. Therefore, when t_{AlN} was 36 nm, a significant portion of the 2 nm-thick ultrathin AlScN layers could be easily damaged and transformed into a non-switchable layer, accelerating the P_r and endurance degradation. Therefore, the maximum t_{AlN} of a-IGZO FeTFT was limited to 30 nm to ensure stable operation.

First, the effects of t_{AlN} on the transfer characteristics in the pristine state were analyzed.

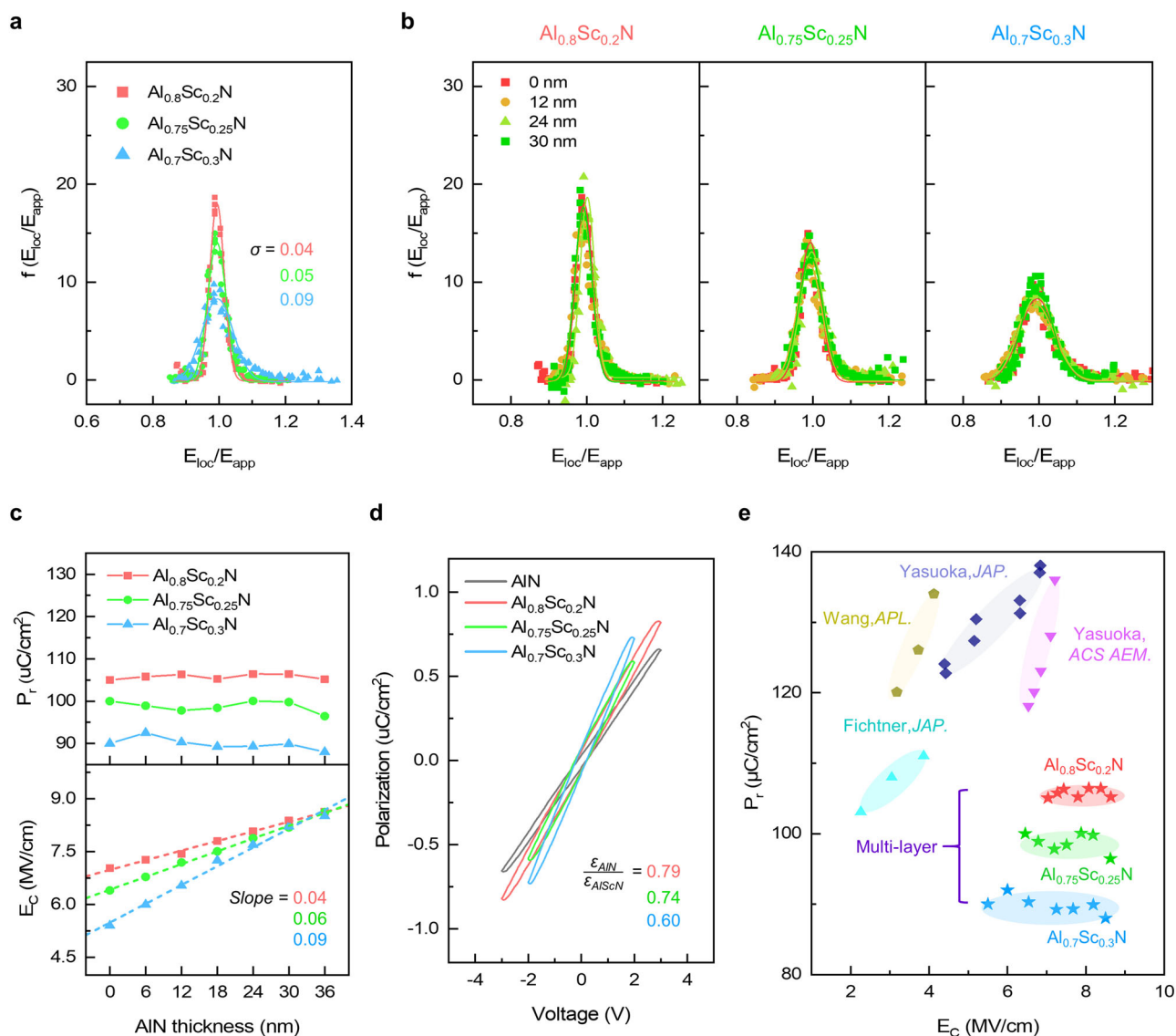


Fig. 3 | Ferroelectric properties of AlScN/AlN/AlScN multi-layer. **a** E_{loc} distribution of the AlScN films, with the standard deviation of the distribution noted. The E_{app} and E_{loc} represent the magnitude of the applied and local electric fields experienced by each domain, respectively. The Sc concentration (x) in $Al_{1-x}Sc_xN$

film was adjusted between 0.2 and 0.3. **b** Changes in E_{loc} distribution of the multi-layer as t_{AlN} varied from 0 to 30 nm. **c** Changes in P_r and E_c of the multi-layer as a function of t_{AlN} . **d** Polarization–voltage curves of the AlN and AlScN films. **e** Benchmark plots of P_r and E_c of AlScN films with varying Sc concentration^{11,19,31,32}.

Supplementary Fig. 10a illustrates the FeTFT in the pristine state, with P_f and σ_t representing the ferroelectric and trapped charge at the AlScN/a-IGZO interface, respectively. If effective charges ($P_f - \sigma_t$) existed at this interface, the threshold voltage (V_{th}) would vary with t_{AlN} due to the decreasing dielectric constant of the multi-layer as t_{AlN} increased (Fig. 4b).

Figure 4c shows the drain current versus gate-to-source voltage ($I_d - V_{gs}$) curve, with a drain-to-source voltage (V_{ds}) of 0.5 V. The channel width (W_{ch}) and length (L_{ch}) were 20 and 3 μm , respectively. V_{th} , extracted at a current level of $(W_{ch}/L_{ch}) \times 10^{-7}$ A, remained constant regardless of t_{AlN} . It has been reported that materials with polar surfaces, such as AlScN, exhibited charge screening effects due to non-stoichiometry and charge modification^{35,36}. Consequently, while AlScN exhibited downward polarization in its pristine state, no effective charges were present at the interface, thereby preventing any significant influence on the V_{th} .

Subsequently, 100-ms-width PGM pulses were applied to the gate, and corresponding V_{th} changes were measured (Fig. 4d). A positive gate voltage was defined as the PGM voltage, following the notation

used in the FeFETs community. As a-IGZO channel is an n-type semiconductor, it provides sufficient electrons to screen positive ferroelectric charges, enabling efficient PGM operation^{37–39}. Supplementary Fig. 10b illustrates FeTFT after PGM operation. Figure 4e shows the $I_d - V_{gs}$ curves as a function of PGM pulse voltage. With increasing PGM pulse amplitude, ferroelectric domains progressively switched upward, resulting in a decrease in V_{th} . Once full switching was achieved, V_{th} saturated, indicating the completion of the PGM operation. V_{th} change before and after PGM (ΔV_{th}) could be expressed by Eq. 2

$$\Delta V_{th} = \frac{\Delta P_f + \Delta \sigma_t}{C_{multi}} \quad (2)$$

where ΔP_f and $\Delta \sigma_t$ represent changes in ferroelectric and trapped charges at the AlScN/a-IGZO interface before and after PGM, and C_{multi} is the capacitance of the multi-layer⁴⁰.

As previously noted, P_r remained constant in the multi-layer regardless of t_{AlN} . Therefore, the charge difference at the AlScN/a-IGZO interface is independent of t_{AlN} . However, as t_{AlN} increased, C_{multi}

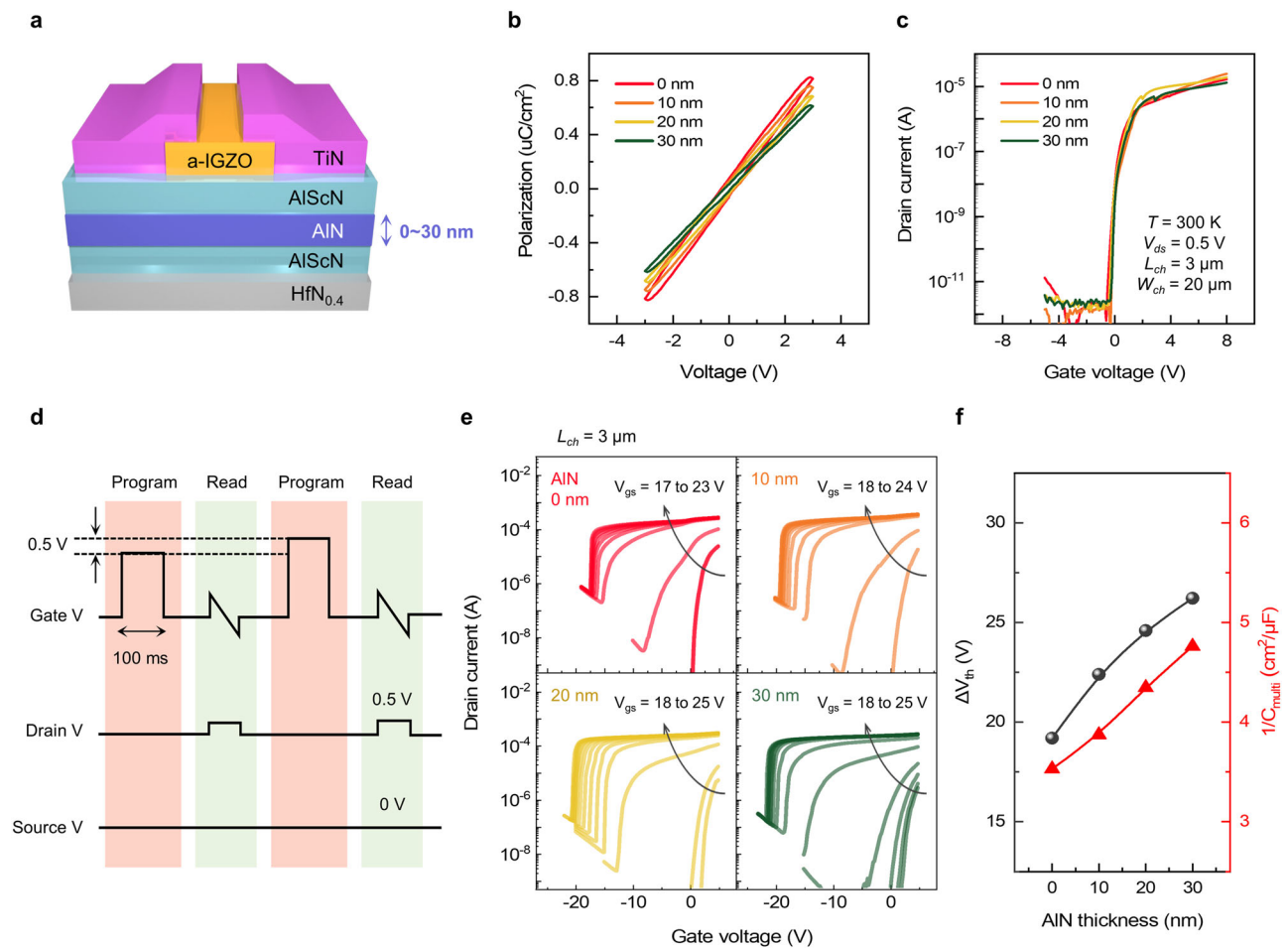


Fig. 4 | Impact of the multi-layer structure on the PGM operation of a-IGZO/AIScN FeTFT. a Schematic illustration of an a-IGZO FeTFT with an AIScN/AIN/AIScN multi-layer. **b** Polarization–voltage curves for multi-layer capacitors with t_{AIN} varying from 0 to 30 nm. **c** Drain current–gate voltage (I_d-V_{gs}) curves for the pristine state, with t_{AIN} varying from 0 to 30 nm. The notation below indicates the

measurement conditions and the dimensions of the FeTFT. **d** Voltage application method used for PGM operation. **e** Changes in I_d-V_{gs} curves as a function of PGM pulse voltage. **f** Changes in the ΔV_{th} and $1/C_{\text{multi}}$ as a function of t_{AIN} . ΔV_{th} and C_{multi} represent the V_{th} shift following PGM operation and the capacitance of the multi-layer, respectively.

decreased, leading to an increase in ΔV_{th} . This relationship was experimentally validated, where ΔV_{th} increased proportionally to $1/C_{\text{multi}}$ (Fig. 4f).

However, a-IGZO/AIScN FeTFT poses a challenge during ERS operation due to insufficient positive charges (hole carriers) in the a-IGZO channel. When applying a negative voltage pulse to the gate for ERS, the electric field is not effectively applied to the ferroelectric layer. Consequently, ferroelectric switching occurs only in localized regions near the source and drain electrodes by the stray field effect^{37,38}.

Supplementary Fig. 11a shows the hysteretic transfer curve for a device with 0 nm t_{AIN} . During the first sweep, downward polarized domains in the pristine state switched under a positive bias, resulting in a counterclockwise hysteresis loop and a large MW exceeding 17 V. However, during the second sweep, the ERS operation failed to switch entire domains due to the lack of hole carriers in the a-IGZO channel, resulting in a negative V_{th} and a decrease in MW. After the sweep was repeated 100 times, the hysteresis curve remained similar to that observed after the second sweep, indicating a stable switching behavior over cycling (Supplementary Fig. 11b). This behavior was consistent across all samples regardless of t_{AIN} (Supplementary Fig. 11c).

Supplementary Fig. 12 shows the V_{th} changes as a function of PGM and ERS pulse amplitudes, and MW was calculated using the saturation points of V_{th} following PGM and ERS operations, denoted as $V_{\text{th,PGM}}$ and $V_{\text{th,ERS}}$, respectively. The effect of pulse width on MW was further investigated by varying the PGM and ERS pulse widths from

100 μs to 100 ms, demonstrating that MW remained constant regardless of the pulse width. Figure 5a shows the variation in the PGM and ERS voltage of FeTFT with 0 nm t_{AIN} as a function of pulse width. Due to the trade-off between pulse width and amplitude for ferroelectric switching, shorter pulses require higher voltages for both PGM and ERS operations⁴¹. Figure 5b shows the MW changes as a function of t_{AIN} . MW increased with t_{AIN} , reaching a maximum of 12 V when t_{AIN} was 30 nm.

To evaluate the device's reliability, endurance, and retention tests were conducted. The pulse schemes for the endurance and retention tests are shown in Supplementary Fig. 13a, b, respectively. Supplementary Fig. 13c shows that all samples, irrespective of t_{AIN} , endured over 10^4 cycles. The ERS state degraded more rapidly than the PGM state, which could be attributed to a preference for the upward polarized state during field cycling⁴². The slightly lower endurance of FeTFT compared to capacitor structures could be attributed to the inferior interface quality between the a-IGZO channel and the AIScN film. All films were deposited in capacitor structures through in-situ sputtering, ensuring clean interfaces. In contrast, the a-IGZO channel in the FeTFT device was ex-situ deposited using sputtering, which could lead to partial oxidation of the AIScN surface, as shown in Supplementary Fig. 14.

Data retention in PGM and ERS states was also measured (Supplementary Fig. 13d). In the device with 0 nm t_{AIN} , MW decreased over time, with only ~84% of the initial MW retained after 10^4 s.

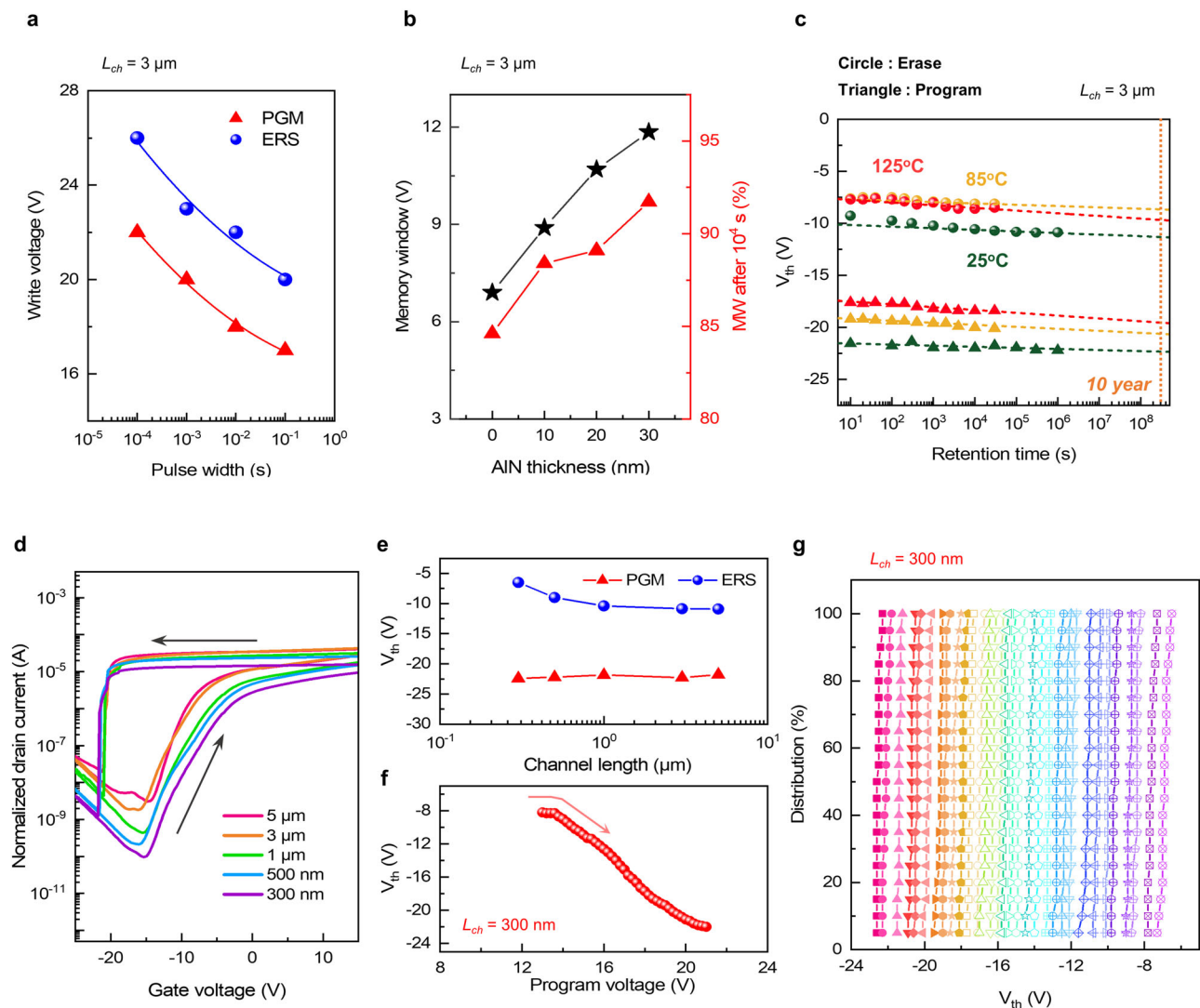


Fig. 5 | Impact of the multi-layer structure on the MW and retention characteristics of FeTFT. a Changes in PGM and ERS pulse voltages required to achieve an identical memory window (MW) at various pulse widths. **b** Effect of t_{AlN} on the MW and retention characteristics of the FeTFT. Retention is compared based on the percentage of MW retained after 10^4 s. **c** Retention characteristics of the FeTFT with

30 nm t_{AlN} at 25, 85, and 125 °C. **d** I_d - V_{gs} hysteresis curves of FeTFTs with varying channel length (L_{ch}) from 300 nm to 5 μm. **e** Changes in the V_{th} of PGM and ERS states for FeTFTs with different L_{ch} . **f** V_{th} evolution of the FeTFT with 300 nm L_{ch} during incremental-step-pulse-programming operation and **g** V_{th} distribution of 32 different states across 20 devices.

However, this degradation was suppressed as t_{AlN} increased. Notably, the device with 30 nm t_{AlN} exhibited stable PGM and ERS states, maintaining MW above 11 V even when extrapolated to 10 years.

This improvement is attributed to the enhanced stability of the multi-layer structure over the depolarization field. Consequently, the device with 30 nm t_{AlN} exhibited the largest MW and superior retention characteristics, demonstrating the multi-layer's capability in both enlarging MW and ensuring long-term stability.

Next, the measurement temperature was increased to evaluate the thermal stability of the device. The device with 30 nm t_{AlN} maintained stable retention characteristics up to 125 °C, as shown in Fig. 5c. Furthermore, even at 185 °C, the FeTFT exhibited stable hysteresis curves over 100 cycles, as shown in Supplementary Fig. 15a, confirming the superior thermal stability. However, significant degradation of the MW was observed during the retention test at 185 °C, with the MW collapsing after 10^4 s (Supplementary Fig. 15b). This degradation could be attributed to a decrease in V_{C} at high temperatures, making the ferroelectric layer vulnerable to the depolarization field and back switching¹².

Additionally, a FeTFT device with a 20 nm-thick multi-layer ($t_{\text{AlN}} = 15$ nm) was fabricated to evaluate the scalability of the AlScN/

AlN/AlScN multi-layer. Although the decreased ferroelectric layer thickness decreased MW to ~8 V, the device still demonstrated excellent retention characteristics, as shown in Supplementary Fig. 16a, b. Moreover, even with a relatively short pulse width of 100 μs, the operation voltages remained below 20 V, comparable to those used in conventional NAND flash memory (Supplementary Fig. 16c)³.

To investigate the impact of L_{ch} on FeTFT performance, devices with 30 nm t_{AlN} were fabricated with L_{ch} ranging from 300 nm to 5 μm. Figure 5d shows the transfer curves for devices, demonstrating counterclockwise hysteresis loops across all L_{ch} . The I_{d} values were normalized by L_{ch} and W_{ch} .

Notably, while $V_{\text{th,PGM}}$ remained relatively constant regardless of L_{ch} , $V_{\text{th,ERS}}$ increased as L_{ch} decreased. V_{th} variations were measured as a function of PGM and ERS pulse amplitudes (Supplementary Fig. 17a) to explore this phenomenon further. Figure 5e shows that, as L_{ch} decreased, $V_{\text{th,ERS}}$ increased, reaching ~6.5 V for a L_{ch} of 300 nm.

This trend can be explained by the distribution of the electric field within the device. In long-channel FeTFTs, the electric field is not effectively applied to the central region of the channel, thereby limiting ferroelectric switching. However, as L_{ch} decreases below a certain

threshold, the stray field affects the entire channel, enabling more effective ERS switching^{37,38}. In contrast, a-IGZO channel consistently provides sufficient electrons regardless of L_{ch} , ensuring consistent $V_{\text{th,PGM}}$. Consequently, shorter L_{ch} enabled more efficient ERS operation, resulting in increased MW. Specifically, for L_{ch} of 300 nm, MW reached -15 V, surpassing the quad-level cell operation threshold and demonstrating the potential for PLC data storage⁴³.

The ISPP method assessed multi-bit feasibility in a 300 nm L_{ch} device with 30 nm t_{AlN} . After erasing the device, 100-ms-width PGM pulses in 0.2 V steps were applied, and the corresponding V_{th} changes were measured. Figure 5f shows the ISPP curve with slopes up to 2, exceeding the theoretical ISPP slope limit of ≤ 1 for CTN-based NAND. This enhanced slope enables efficient and disturbance-free multi-level operation. As shown in Supplementary Fig. 17b, the program pulse width could be decreased to 1 μs at the expense of increased program voltage. Supplementary Fig. 17c shows 32 distinct memory states identified through ISPP, with an average voltage separation of 0.5 V. Figure 5g shows a tight distribution of these states across 20 devices, demonstrating the PLC feasibility and uniformity. Supplementary Table 2 shows benchmark results compared with reported AlScN-based FeFETs, highlighting the superior performance of the device.

Discussion

This study introduced an AlScN/AlN/AlScN multi-layer ferroelectric material, where the ferroelectric switching of the upper and lower AlScN layers ferroelectrically switches the interposed AlN layer between AlScN films. However, the AlN has a lower dielectric constant than AlScN, enabling the modulation of E_{C} without altering the P_{r} by changing the AlN ratio. Such decoupling significantly enhanced the design flexibility of wurtzite-structured ferroelectrics, expanding their adaptability to diverse device applications.

The FeTFTs with an a-IGZO channel and this multi-layer gate stack demonstrated significantly improved MW and retention characteristics. Furthermore, the ISPP method validated the PLC operation, achieving 32 distinct states. This capability highlights the potential of AlScN-based FeFETs as a promising alternative to conventional NAND devices, opening up new possibilities for future memory technologies.

Methods

HfN_{0.4}/AlScN/AlN/AlScN/TiN capacitor fabrication

The HfN_{0.4} BE was deposited onto a Si/SiO₂ substrate using radio frequency (RF) reactive sputtering with an Hf metal target. The sputtering process was conducted at a power of 400 W, a working pressure of 2 mTorr, and a gas flow of 19 sccm of Ar and 1 sccm of N₂. Subsequently, an AlScN film was deposited via RF reactive magnetron sputtering using AlN and Sc metal targets. The sputtering powers for the AlN and Sc targets were set at 290 W and 210 W, respectively. This deposition process was performed under a working pressure of 20 mTorr with a N₂ gas flow of 20 sccm. Following the AlScN deposition, a TiN TE was deposited via direct current (DC) reactive sputtering. The sputtering conditions included a power setting of 400 W, a working pressure of 2 mTorr, and an N₂ gas flow of 20 sccm. All films were deposited at room temperature without breaking the vacuum. Following the TiN film deposition, the circular TE with an area of 640 μm^2 was patterned using photolithography (DL-1000 HP, Nano-System Solutions) and a dry etching (Plasma Pro System 100 Cobra, Oxford Instrument) process. Details of these capacitor fabrication processes and thickness scalability were reported elsewhere^{21,44}.

amorphous-IGZO/AlScN/AlN/AlScN FeTFT fabrication

The HfN_{0.4}/AlScN/AlN/AlScN stack was deposited onto a Si/SiO₂ substrate using RF sputtering, following the process for the capacitor fabrication. Then, a 20 nm-thick a-IGZO film was ex-situ deposited via RF magnetron sputtering using a ceramic target with the In:Ga:Zn ratio of 1:1:1 under conditions of 300 W power, 5 mTorr working pressure,

and a gas flow of 60 sccm Ar at room temperature. The a-IGZO thin film was patterned using photolithography and wet-etched in a diluted hydrofluoric acid solution to define the channel area. Subsequently, the source and drain contacts were patterned using photolithography, and a 100-nm-thick TiN layer was deposited via DC sputtering, followed by a lift-off process. Finally, furnace annealing was performed at 350 °C in ambient air to mitigate the damage caused by the TiN source/drain electrode deposition and improve the contact properties.

TiN/HZO/HO/HZO/TiN capacitor fabrication

A 50 nm-thick TiN BE was deposited on a Si/SiO₂ substrate using DC sputtering. HZO and HO films were deposited using thermal atomic layer deposition (Atomic-Classical, CN-1) at a substrate temperature of 285 °C. Hf[N(C₂H₅)CH₃]₄ (TEMA-Hf), Zr[N(C₂H₅)CH₃]₄ (TEMA-Zr), and ozone were used as the Hf, Zr, and oxygen sources, respectively. The TiN TE was deposited via DC sputtering and patterned using a shadow mask to define an area of 120,000 μm^2 .

Characterization

The thicknesses of the AlN and AlScN films were determined using spectroscopic ellipsometry (M-2000, J.A. Woollam). The films' crystalline quality and elemental composition were characterized using XRD (X'pert Pro, PANalytical) and HRTEM (JEM-2100F, JEOL Ltd). The polarization direction of the film was analyzed using STEM (Titan Themis G2 300, FEI). The electrical characteristics of the devices were measured using a semiconductor characterization system (4200A-SCS, Keithley). All measurements were conducted in air at room temperature.

Data availability

All data that support the findings of this work are included in the article and Supplementary Information. The raw data are not publicly available due to intellectual property restrictions, but can be obtained from the corresponding author upon reasonable request.

References

1. Tanaka, T. et al. A 768Gb 3b/cell 3D-floating-gate NAND flash memory. In *Proc. 2016 IEEE International Solid-State Circuits Conference (ISSCC)* 142–144 (IEEE, 2016).
2. Khatri, S. P. et al. In *Frontiers of Quality Electronic Design (QED) AI, IoT and Hardware Security* 67–136 (Springer, 2022).
3. Kim, S. S. et al. Review of semiconductor flash memory devices for material and process issues. *Adv. Mater.* **35**, 2200659 (2023).
4. Mielke, N. R. et al. Reliability of solid-state drives based on NAND flash memory. *Proc. IEEE* **105**, 1725–1750 (2017).
5. Dong, G., Li, S. & Zhang, T. Using data postcompensation and pre-distortion to tolerate cell-to-cell interference in MLC NAND flash memory. *IEEE Trans. Circuits Syst. I Regul. Pap.* **57**, 2718–2728 (2010).
6. Park, H. W., Lee, J. G. & Hwang, C. S. Review of ferroelectric field-effect transistors for three-dimensional storage applications. *Nano Sel.* **2**, 1187–1207 (2021).
7. Kim, J. Y., Choi, M.-J. & Jang, H. W. Ferroelectric field effect transistors: progress and perspective. *APL Mater.* **9**, 021102 (2021).
8. Mulaosmanovic, H. et al. Ferroelectric field-effect transistors based on HfO₂: a review. *Nanotechnology* **32**, 502002 (2021).
9. Hachiya, S., Johguchi, K., Miyaji, K. & Takeuchi, K. Hybrid triple-level-cell/multi-level-cell NAND flash storage array with chip exchangeable method. *Jpn. J. Appl. Phys.* **53**, 04EE04 (2014).
10. Park, K.-T. et al. A fully performance compatible 45 nm 4-gigabit three-dimensional double-stacked multi-level NAND flash memory with shared bit-line structure. *IEEE J. Solid State Circuits* **44**, 208–216 (2008).
11. Fichtner, S., Wolff, N., Lofink, F., Kienle, L. & Wagner, B. AlScN: a III-V semiconductor based ferroelectric. *J. Appl. Phys.* **125**, 114103 (2019).
12. Pradhan, D. K. et al. A scalable ferroelectric non-volatile memory operating at 600° C. *Nat. Electron.* **7**, 348–355 (2024).

13. Islam, M. R. et al. On the exceptional temperature stability of ferroelectric $\text{Al}_{1-x}\text{Sc}_x\text{N}$ thin films. *Appl. Phys. Lett.* **118**, 232905 (2021).
14. Kim, K. D. et al. Influences of the inhomogeneity of the ferroelectric thin films on switching current. *MRS Commun.* **13**, 825–833 (2023).
15. Kim, K.-H. et al. Scalable CMOS back-end-of-line-compatible AlScN/two-dimensional channel ferroelectric field-effect transistors. *Nat. Nanotechnol.* **18**, 1044–1050 (2023).
16. Song, S. et al. High current and carrier densities in 2D $\text{MoS}_2/\text{AlScN}$ field-effect transistors via ferroelectric gating and ohmic contacts. *ACS Nano* **19**, 8985–8996 (2025).
17. Liao, C.-Y. et al. Mechanisms of instability retention for ferroelectric field-effect transistors with HfZrO_2 gate stack scaling down. *Appl. Phys. Lett.* **121**, 252902 (2022).
18. Kim, K. D. et al. Comparative study on the stability of ferroelectric polarization of HfZrO_2 and AlScN thin films over the depolarization effect. *J. Appl. Phys.* **136**, 024101 (2024).
19. Yasuoka, S. et al. Effects of deposition conditions on the ferroelectric properties of $(\text{Al}_{1-x}\text{Sc}_x)\text{N}$ thin films. *J. Appl. Phys.* **128**, 114103 (2020).
20. Ye, K. H., Han, G., Yeu, I. W., Hwang, C. S. & Choi, J.-H. Atomistic understanding of the ferroelectric properties of a wurtzite-structure $(\text{AlN})_n/(\text{ScN})_m$ superlattice. *Phys. Status Solidi Rapid Res. Lett.* **15**, 2100009 (2021).
21. Ryoo, S. K. et al. Fabrication of ultrathin ferroelectric $\text{Al}_{0.7}\text{Sc}_{0.3}\text{N}$ films under complementary-metal-oxide-semiconductor compatible conditions by using $\text{HfN}_{0.4}$ electrode. *Adv. Mater.* **37**, 2413295 (2025).
22. Liu, X. et al. Aluminum scandium nitride-based metal–ferroelectric–metal diode memory devices with high on/off ratios. *Appl. Phys. Lett.* **118**, 202901 (2021).
23. Wong, Z. M., Wu, G. & Hariharaputran, R. Unravelling the polarity preference and effects of the electrode layer on wurtzite aluminum nitride for piezoelectric applications. *Mater. Adv.* **5**, 3289–3296 (2024).
24. Stolyarchuk, N. et al. Intentional polarity conversion of AlN epitaxial layers by oxygen. *Sci. Rep.* **8**, 14111 (2018).
25. Skidmore, C. H. et al. Proximity ferroelectricity in wurtzite heterostructures. *Nature* **637**, 574–579 (2025).
26. Zhukov, S. et al. Dynamics of polarization reversal in virgin and fatigued ferroelectric ceramics by inhomogeneous field mechanism. *Phys. Rev. B Condens. Matter Mater. Phys.* **82**, 014109 (2010).
27. Kim, K. D. et al. Evolution of the ferroelectric properties of AlScN film by electrical cycling with an inhomogeneous field distribution. *Adv. Electron. Mater.* **9**, 2201142 (2023).
28. Schütrumpf, J., Zhukov, S., Genenko, Y. A. & Von Seggern, H. Polarization switching dynamics by inhomogeneous field mechanism in ferroelectric polymers. *J. Phys. D Appl. Phys.* **45**, 165301 (2012).
29. Wingqvist, G. et al. Increased electromechanical coupling in $\text{w-Sc}_x\text{Al}_{1-x}\text{N}$. *Appl. Phys. Lett.* **97**, 112902 (2010).
30. Park, H. W. et al. Polarizing and depolarizing charge injection through a thin dielectric layer in a ferroelectric–dielectric bilayer. *Nanoscale* **13**, 2556–2572 (2021).
31. Yasuoka, S. et al. Tunable ferroelectric properties in wurtzite $(\text{Al}_{0.8}\text{Sc}_{0.2})\text{N}$ via crystal anisotropy. *ACS Appl. Electron. Mater.* **4**, 5165–5170 (2022).
32. Wang, P. et al. Fully epitaxial ferroelectric ScAlN grown by molecular beam epitaxy. *Appl. Phys. Lett.* **118**, 223504 (2021).
33. Dou, X. et al. Polarization switching pathways of ferroelectric Zr-doped HfO_2 based on the first-principles calculation. *Appl. Phys. Lett.* **124**, 092901 (2024).
34. Park, M. H. et al. Ferroelectricity and antiferroelectricity of doped thin HfO_2 -based films. *Adv. Mater.* **27**, 1811–1831 (2015).
35. Hong, S., Nakhmanson, S. M. & Fong, D. D. Screening mechanisms at polar oxide heterointerfaces. *Rep. Prog. Phys.* **79**, 076501 (2016).
36. Mora-Fonz, D. et al. Why are polar surfaces of ZnO stable?. *Chem. Mater.* **29**, 5306–5320 (2017).
37. Mo, F., Mei, X., Saraya, T., Hiramoto, T. & Kobayashi, M. A simulation study on memory characteristics of InGaZnO-channel ferroelectric FETs with 2D planar and 3D structures. *Jpn. J. Appl. Phys.* **61**, SC1013 (2022).
38. Lee, J. H. et al. Gate engineering effect in ferroelectric field-effect transistors with Al-doped HfO_2 thin film and amorphous indium-gallium-zinc-oxide channel. *Adv. Electron. Mater.* **11**, 2400516 (2025).
39. Park, J. S., Maeng, W.-J., Kim, H.-S. & Park, J.-S. Review of recent developments in amorphous oxide semiconductor thin-film transistor devices. *Thin Solid Films* **520**, 1679–1693 (2012).
40. Kim, G. et al. Experimental analysis on the interaction between interface trap charges and polarization on the memory window of metal–ferroelectric–insulator–Si (MFIS) FeFET. *IEEE Trans. Electron Devices* **71**, 6627–6632 (2024).
41. Ishibashi, Y. & Takagi, Y. Note on ferroelectric domain switching. *J. Phys. Soc. Jpn.* **31**, 506–510 (1971).
42. Shao, Y. et al. Discrete ferroelectric polarization switching in nanoscale oxide-channel ferroelectric field-effect transistors. *Nano Lett.* **25**, 3173–3179 (2025).
43. Das, D. et al. Design framework for ferroelectric gate stack engineering of vertical NAND structures for efficient TLC and QLC operation. In *Proc. 2024 IEEE International Memory Workshop (IMW)* 1–4 (IEEE, 2024).
44. Ryoo, S. K. et al. Investigation of optimum deposition conditions of radio frequency reactive magnetron sputtering of $\text{Al}_{0.7}\text{Sc}_{0.3}\text{N}$ film with thickness down to 20 nm. *Adv. Electron. Mater.* **8**, 2200726 (2022).

Acknowledgements

This work was supported by the National Research Foundation of Korea (Grant No. 2020R1A3B2079882).

Author contributions

K.D.K. optimized the sputtering process, fabricated the devices, and conducted electrical measurements. S.K.R., M.K.Y. and S.H.L. contributed to the hardware maintenance of the sputter. W.C. assisted in organizing the manuscript figures. Y.K. supported the analysis of switching characteristics of a multi-layer structure supervised by J.H.C. T.X. performed the STEM analysis supervised by Y.C. K.D.K. and C.S.H. wrote the manuscript. C.S.H. supervised the entire research project. All authors reviewed, discussed, and approved the final manuscript.

Competing interests

The authors declare no competing interests.

Additional information

Supplementary information The online version contains supplementary material available at <https://doi.org/10.1038/s41467-025-62904-6>.

Correspondence and requests for materials should be addressed to Cheol Seong Hwang.

Peer review information *Nature Communications* thanks Huake Su and the other, anonymous, reviewer(s) for their contribution to the peer review of this work. A peer review file is available.

Reprints and permissions information is available at <http://www.nature.com/reprints>

Publisher's note Springer Nature remains neutral with regard to jurisdictional claims in published maps and institutional affiliations.

Open Access This article is licensed under a Creative Commons Attribution-NonCommercial-NoDerivatives 4.0 International License, which permits any non-commercial use, sharing, distribution and reproduction in any medium or format, as long as you give appropriate credit to the original author(s) and the source, provide a link to the Creative Commons licence, and indicate if you modified the licensed material. You do not have permission under this licence to share adapted material derived from this article or parts of it. The images or other third party material in this article are included in the article's Creative Commons licence, unless indicated otherwise in a credit line to the material. If material is not included in the article's Creative Commons licence and your intended use is not permitted by statutory regulation or exceeds the permitted use, you will need to obtain permission directly from the copyright holder. To view a copy of this licence, visit <http://creativecommons.org/licenses/by-nc-nd/4.0/>.

© The Author(s) 2025